Technical University of Munich
Department of Physics

FOPRA 34

Simulating Quantum Many-Body Dynamics on a Current Digital Quantum Computer

Patrick Hopf, Philipp Thoma, Daniel Ortmann

July 2023

Contents

1 Introduction

In this project we simulate the quantum many-body dynamics on a current digital quantum computer using Qiskit.

2 Day 1

2.1 Exercise 1

Since P_{ab} is a conditional probability (conditioned on b), $\sum_a P_{ab} = 1$ for all $b \in \{1, ..., 2^N\}$. Hence,

$$\sum_b v_b = \sum_{a,b} P_{ab}\, v_b = \sum_a v'_a = 1.$$

2.2 Exercise 2

The quantum teleportation protocol enables the transfer of quantum information from one qubit to another, using a shared entangled pair of qubits. A common basis for such entangled states is defined by the four Bell states and can be produced using the circuits displayed in Figure 1.

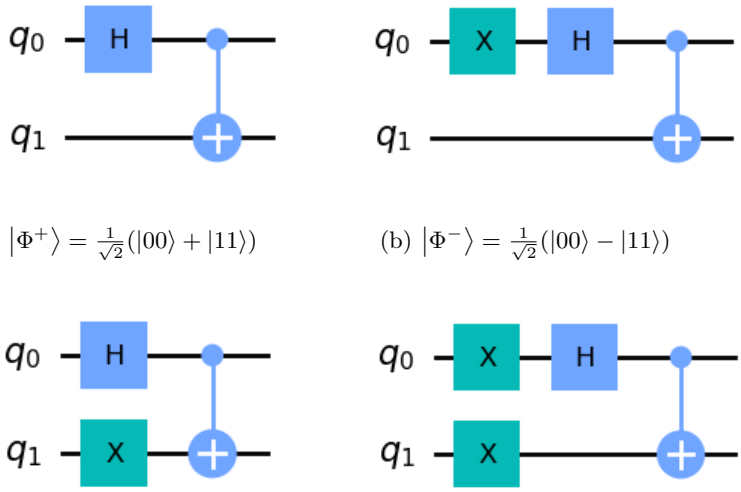

(a) $\left|\Phi^+\right\rangle = \frac{1}{\sqrt{2}}(|00\rangle + |11\rangle)$ (b) $\left|\Phi^-\right\rangle = \frac{1}{\sqrt{2}}(|00\rangle - |11\rangle)$

(c) $\left|\Psi^+\right\rangle = \frac{1}{\sqrt{2}}(|01\rangle + |10\rangle)$ (d) $\left|\Psi^-\right\rangle = \frac{1}{\sqrt{2}}(|01\rangle - |10\rangle)$

Figure 1: Two qubit circuits, which produce the four EPR pairs.

The function of those circuits can be summarized for input qubits q_0 and q_1 as

$$|\beta(q_0, q_1)\rangle = \frac{1}{\sqrt{2}}\left(|0, q_1\rangle + (-1)^{q_0}\,|1, 1 - q_1\rangle\right). \tag{1}$$

2.3 Exercise 3

To implement the teleportation protocol, our three qubit circuit prepares the input state (message) and produces a EPR pair in the second (sender) and third (receiver) qubit. A Bell measurement is then performed on the senders entangled qubit and the input qubit. Based on the measurement results, conditional X and Z operations are performed on the target qubit to reproduce the state of the input qubit. If the sender's Bell measurement outcome is $|\Phi^+\rangle \rightarrow 00$, no operation is applied to the receiver's qubit. If the outcome is $|\Phi^-\rangle \rightarrow 01$, the receiver's qubit is flipped (bit-flip operation) using an X gate. If the outcome is $|\Psi^+\rangle \rightarrow 10$, the receiver's qubit undergoes a phase-flip operation (Z gate). If the outcome is $|\Psi^-\rangle \rightarrow 11$, the receiver's qubit undergoes a bit-flip operation (X gate) and a phase-flip operation (Z gate followed by X gate). This procedure achieves therefore teleportation of the message qubit to the receivers qubit, where the conditional operations can be regarded as classical message transmission.

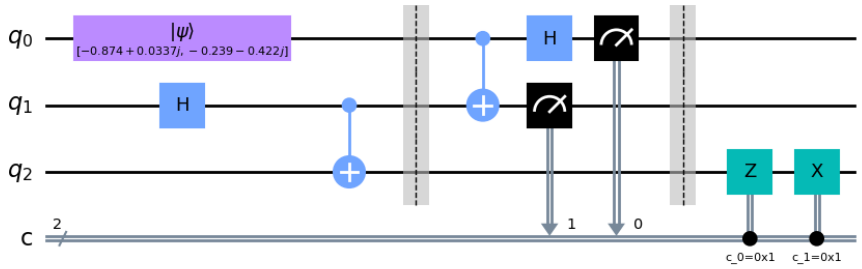

Figure 2: Quantum teleportation circuit with input/message qubit q_0, sender q_1 and receiver q_2. Preparation of random input state and Bell $|\Phi^+\rangle$ state followed by Bell measurement and conditional operations after 'classical' communication of measurement results.

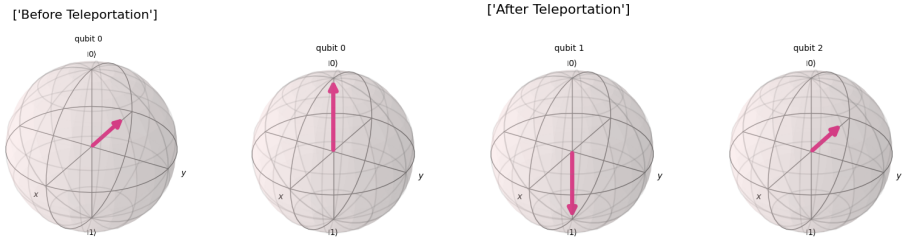

(a) random message q_0 (b) message q_0, sender q_1, receiver q_2

Figure 3: Random state initially at q_0, teleported to q_2. After simulating procedure both sender and message qubit are collapsed due to the Bell measurement.

2.4 Exercise 4

Under a time-dependent transverse **B**-field, the single qubit Hamiltonian is given by

$$\hat{H} = -\frac{\omega_0}{2}\hat{\sigma}_z + \omega_1 \cos(\omega t)\hat{\sigma}_x, \tag{2}$$

and leads to a rotation on the Bloch sphere

$$\begin{aligned} |\Psi\rangle &= \alpha(t)\,|0\rangle + \beta(t)\,|1\rangle \\ &= \mathrm{e}^{\mathrm{i}\omega t/2}\left(\cos\left(\tfrac{\Omega t}{2}\right) - \tfrac{\mathrm{i}\Delta}{\Omega}\sin\left(\tfrac{\Omega t}{2}\right)\right)|0\rangle - \mathrm{e}^{-\mathrm{i}\omega t/2}\tfrac{\mathrm{i}\omega_1}{\Omega}\sin\left(\tfrac{\Omega t}{2}\right)|1\rangle\,. \end{aligned} \tag{3}$$

The oscillating population of state $|0\rangle$ and $|1\rangle$ are then given by the abolute squared values:

$$\begin{aligned} P(|0\rangle) &= \cos^2(\tfrac{\Omega t}{2}) + \tfrac{\Delta^2}{\Omega^2}\sin^2(\tfrac{\Omega t}{2}) \\ P(|1\rangle) &= \tfrac{\omega_1^2}{\Omega^2}\sin^2(\tfrac{\Omega t}{2}). \end{aligned} \tag{4}$$

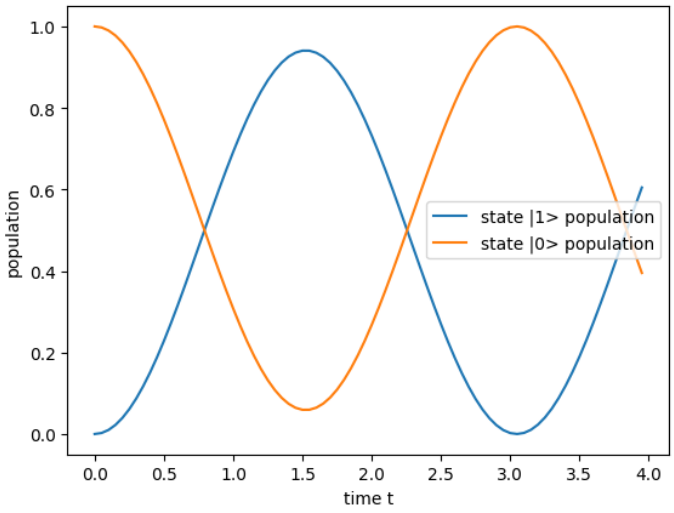

Figure 4: Oscillating population of $|0\rangle$ and $|1\rangle$ states for a qubit subject to a time-dependent magnetic field.

2.5 Exercise 5

To implement the evolution of the Hamiltonian (2) as quantum circuit, we use the Trotterization $\mathcal{T}$ technique to decompose the unitary

$$\begin{aligned} \hat{U}(t) &= \mathcal{T}\left(\exp\left(\mathrm{i}\int_0^t \hat{H}(t)\mathrm{d}t\right)\right) \\ &\approx \prod_{n=0}^{N}\exp\left(\tfrac{\mathrm{i}\omega_0\delta t}{2}\sigma_z\right)\exp(-\mathrm{i}\omega_1\delta t\cos(\omega n\delta t)\sigma_x). \end{aligned} \tag{5}$$

For fixed frequencies of $\omega = 25.5$ and $\omega_0 = 25 \gg \omega_1 = 2$ (s. Figure 5a orange line) the measurement of the circuit output over 400 shots for each timestep gives rise to a population which closely resembles the expected oscillatory pattern we calculated from the amplitude in equation (3). The analytically obtained solution however does no longer describe the correct physical behaviour for $\omega_1 = \omega_0$ (s. Figure 5a blue line), since the RWA only holds in the regime of $\omega_1 \ll \omega_0$ and $\Delta = \omega - \omega_0 \approx 0$. Here the trotterized circuit measurement better represent the correct qubit behaviour. For varying frequency we measure a maximum population at $t = \pi/\omega_1 = \pi/2$ as the frequency approaches $\omega = 25 = \omega_0$.

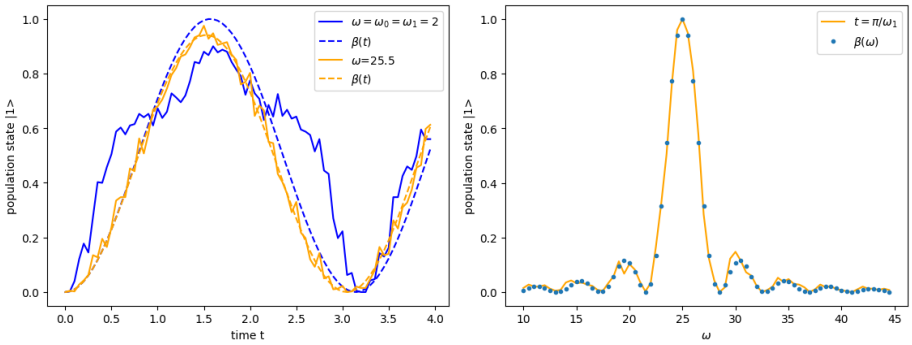

(a) fixed frequency ω (b) fixed time t

Figure 5: Population of state $|1\rangle$ extracted from a 400 shot measurement of trotterized circuit compared to analytically obtained solution.

2.6 Exercise 6

Introducing the generalized amplitude damping quantum channel (GAD) into our measurement simulations, we observe an exponential decay envelope in the oscillating population of state $|1\rangle$. This so-called decoherence is leading to a loss of quantum information.

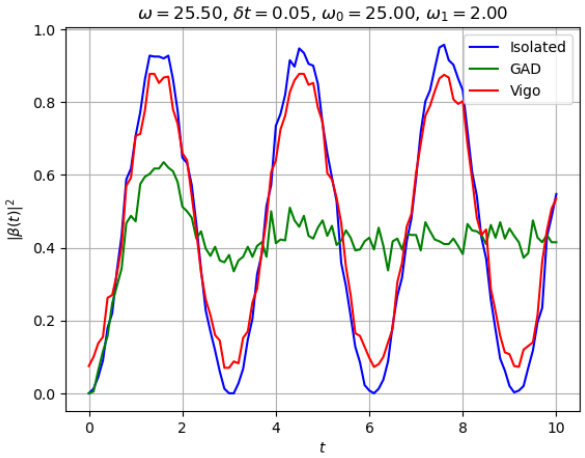

Figure 6: Comparision between time dependent population of $|1\rangle$ state for measurement with, without GAD noise model ($\delta t = 0.05$) and simulation of a real quantum computer.

2.7 Exercise 7

The dampening due to the GAD noise model with parameters of $p = 0.1$ and $\gamma = 0.02$ shows even greater reduction in the maximum state population as a simulated fake backend wich models the typical errors of IBMs Vigo quantum computer. Due to the application of the error channel after each gate and the subsequent increase in circuit length with smaller δt, the influence of decoherence, especially spontaneous emission, becomes more dominant for smaller δt. Remarkably, when δt is set to 0.01, no observable oscillation occurs, and the system quickly reaches the steady state solution (s. Figure 7). Conversely, when δt is set to 0.05, we still observe an exponentially decaying oscillation. It is worth noting that Vigo displays notable resilience against the effects of decoherence.

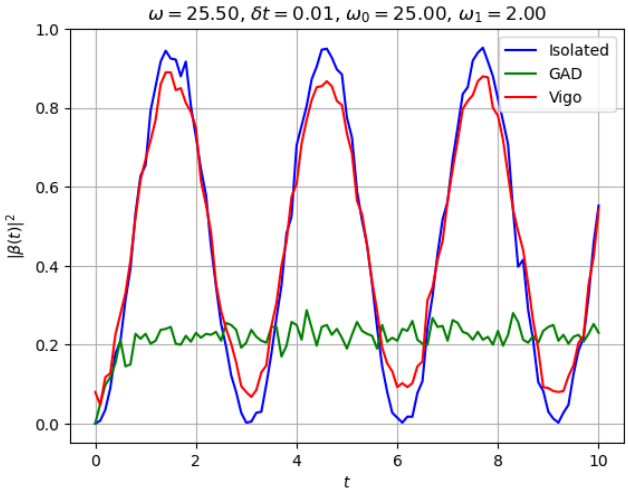

Figure 7: Comparision between time dependent population of $|1\rangle$ state for measurement with, without GAD noise model ($\delta t 0.01$) and simulation of a real quantum computer.

2.8 Exercise 8

The identities $X = HZH$ and $Y = SHZHS^\dagger$ can be easily verified by straightforward matrix multiplication. To measure $|\psi\rangle$ in the $X-$ and $Y-$basis, we simply compute $H\psi$ and $HS^\dagger\psi$, respectively, and measure in the $Z-$basis.

2.9 Exercise 9

Note that the spectrum of $\rho = \frac{1}{2}I + \vec{c}\cdot\vec{\sigma}$ is $\text{spec}(\rho) = \{\frac{1}{2} \pm |\vec{c}|\}$. For ρ to be a valid quantum state $\rho \geq 0$ must hold. However, since we perform a finite number of measurements, we only get an approximation $2\vec{c}' \approx \langle\vec{\sigma}\rangle$ and thus $|\vec{c}'| \leq \frac{1}{2}$ might not be fulfilled anymore. If $|\vec{c}'| > \frac{1}{2}$, we re-normalize to $\vec{c} = \vec{c}'/2|\vec{c}'|$

to obtain a valid density matrix. Assuming $\rho = |\psi\rangle\langle\psi|$ for some pure state $|\psi\rangle = \alpha|0\rangle + \beta|1\rangle \cong |\alpha||0\rangle + |\beta|e^{i(\phi(\beta)-\phi(\alpha))}|1\rangle$, we extract α and β up to some global phase $e^{i\phi(\alpha)}$ by calculating

$$|\alpha| = \sqrt{1/2 + c_3} \qquad |\beta| = \sqrt{1/2 - c_3} \qquad \phi(\beta) - \phi(\alpha) = \phi(c_1 + ic_2)$$

Note that $\phi(z)$ denotes the phase of $z \in \mathbb{C}$.

2.10 Exercise 10

As expected, RWA is in good agreement with the qubit dynamic extracted via state tomography (cf. Figure 8).

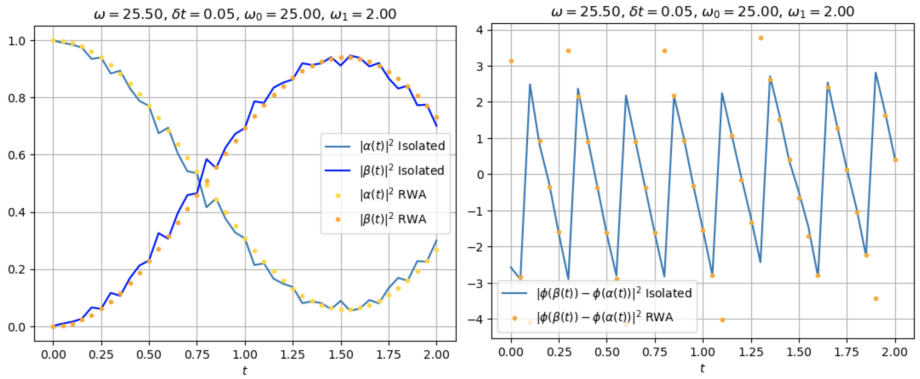

(a) (b)

Figure 8: Comparison of $\alpha(t)$ and $\beta(t)$ between RWA and qubit dynamic extracted via state tomography.

2.11 Exercise 11

The VQE ansatz circuit preparing $|\psi(a,b)\rangle$ for $a, b \in [0, \pi]$ is given by

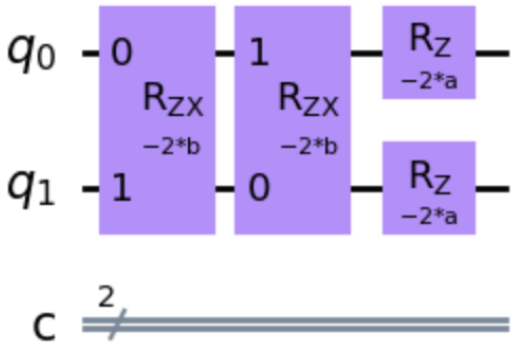

Figure 9: Ansatz circuit for VQE.

2.12 Exercise 12

The heatmap (cf. Figure 10) implies that the ansatz circuit has a symmetry as it is invariant under $(a,\ b) \to (a+\pi/2,\ b+\pi/2)$, which corresponds to additional $\pi-$rotations. The dark and light circular regions correspond to the eigenvalues -2 and $+2$, respectively. We measure for the ground state $|\psi(0.83, 0.83)\rangle$ with a ground state energy of -2.

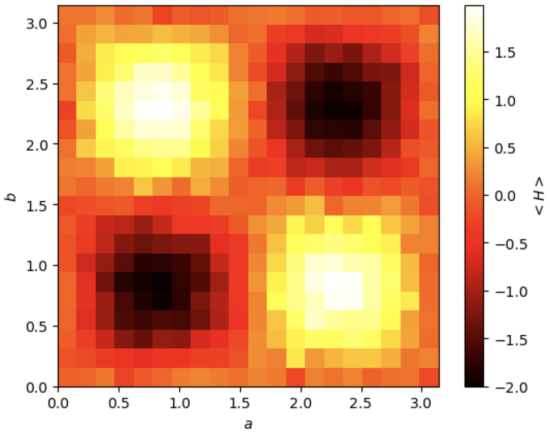

Figure 10: Measured energy for parameters $a, b \in [0, \pi]$.

2.13 Exercise 13

Indeed, $H|\psi\rangle = -\frac{1}{\sqrt{2}}(|0,+\rangle + |1,-\rangle + |1,-\rangle + |0,+\rangle) = -2|\psi\rangle$. In the standard basis $|\psi\rangle = (1, 1, 1, -1)/2$. Computing the inner product $\langle\psi(0.83, 0.83)|\psi\rangle$ gives approximately one as expected.

2.14 Exercise 14

Adding GAD noise with $\gamma = 0.1$ and $p = 0.2$ blurs the energy landscape slightly out (cf. Figure 11). The exact ground state (i.e. without noise) should be approximately at (0.83, 0.83) or, due to the symmetry, at (2.31, 2.31). We measure for the ground state $|\psi(2.31, 2.65)\rangle$ with a ground state energy of -1.24. As expected, the noise channels map the exact ground state to different (a', b') near the true values (a, b). For the overlap between measured ground state and exact ground state, we compute $\langle\psi(2.31, 2.65)|\psi\rangle \approx 0.91$.

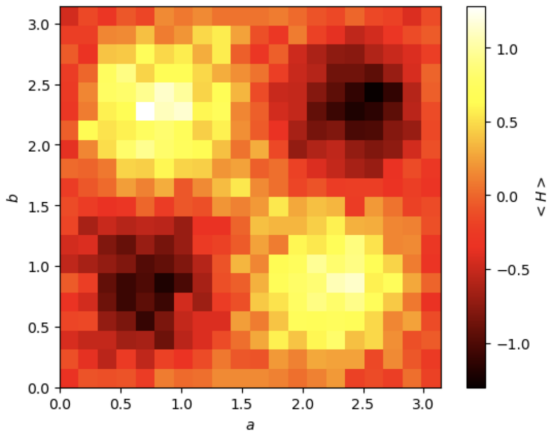

Figure 11: Measured energy for parameters $a, b \in [0, \pi]$ with GAD noise channel using $\gamma = 0.1, p = 0.2$.

3 Day 2

3.1 Exercise 1

The exponential growth of $\mathcal{G}(t)$ and $\mathcal{L}(t)$ is applicable solely when the quench modifies the energy density of the system. This bears similarity to the thermal excitation observed in Boltzmann statistics, where the system occupies each eigenstate with equal probability when the temperature is sufficiently high. Consequently, as the system progresses over time, the likelihood of it returning to the same initial state vanishes exponentially towards zero. The following equality holds

$$\lambda(t) = -\frac{1}{N}\ln|\mathcal{G}(t)|^2 = -\frac{1}{N}\ln\left|\mathrm{e}^{-Ng(t)}\right|^2 = -\frac{1}{N}\ln\left(\mathrm{e}^{-2N\mathrm{Re}[g(t)]}\right) = 2\mathrm{Re}[g(t)]. \tag{6}$$

3.2 Exercise 2

$$\begin{aligned}
\lim_{N\to\infty}\lambda(t) &= \lim_{N\to\infty} -\frac{1}{N}\log\mathcal{L}(t) \\
&= \lim_{N\to\infty} -\frac{1}{N}\log\left(\sum_i \mathrm{e}^{-N\lambda_i(t)}\right) \\
&\overset{\text{L.H.}}{=} \lim_{N\to\infty}\frac{\sum_i \lambda_i(t)e^{-N\lambda_i(t)}}{\sum_i e^{-N\lambda_i(t)}} \\
&= \sum_i \lambda_i(t)\lim_{N\to\infty}\frac{1}{\sum_{\lambda_j(t)<\lambda_i(t)} e^{N(\lambda_i(t)-\lambda_j(t))} + 1 + \sum_{\lambda_j(t)>\lambda_i(t)} e^{N(\lambda_i(t)-\lambda_j(t))}} \\
&= \sum_i \lambda_i(t)\lim_{N\to\infty}\frac{1}{\sum_{\lambda_j(t)<\lambda_i(t)} e^{N(\lambda_i(t)-\lambda_j(t))} + 1} \\
&= \min_i \lambda_i
\end{aligned}$$

The last equal signs holds, since the divergent term in denominator vanishes only for the minimum λ_i as an empty sum.

3.3 Exercise 3

To calculate the commutator between Hamiltonian $\hat{H}$ and parity operator $\hat{P}$

$$[\hat{H},\hat{P}] = -\frac{1}{2}\left[\sum_{<i,j>} Z_iZ_j, X_0X_1\ldots X_n\right] - \frac{g}{2}\left[\sum_i X_i, X_0X_1\ldots X_n\right] \tag{7}$$

where Z_iZ_j corresponds to the Pauli matrices with respect to the lattice sites i and j:

$$Z_iZ_j = \mathbf{1}_1\otimes\mathbf{1}_2\otimes\cdots\otimes Z_i\otimes\mathbf{1}_{i+1}\otimes\cdots\otimes Z_j\otimes\mathbf{1}_{j+1}\otimes\cdots\otimes\mathbf{1}_L, \tag{8}$$

we make use of their commutator relations

$$(Z_i \otimes Z_j)(X_i \otimes X_j) = (Z_i X_i) \otimes (Z_j X_j) = (-1)(X_i Z_i) \otimes (-1)(X_j Z_j) = (X_i \otimes X_j)(Z_i \otimes Z_j), \tag{9}$$

to obtain

$$P\,(Z_i Z_j) = \left(\prod_{l \neq i,j} X_l \right) (X_i X_j)(Z_i Z_j) = (Z_i Z_j) \left(\prod_{l \neq i,j} X_l \right) (X_i X_j) = (Z_i Z_j) P. \tag{10}$$

We used the fact that operators on different lattice sites (i.e. different indices) always commute with each other. Thus together with $X_i X_i = \mathbf{1}$ we see that X_i commutes with P and, the second part $-\frac{g}{2}\left[\sum_i X_i, X_0 X_1 \dots X_n\right]$ of equation (7) becomes zero.

For $g = 0$, the two-dimensional ground state manifold is $\langle\, |0 \dots . 0\rangle\,,\, |1 \dots . 1\rangle\rangle$. For $g \to \infty$ the ground state is given by $|+ \dots . +\rangle$. Consequently, the magnetization is

$$\langle m_z \rangle = \begin{cases} \pm 1, & g = 0 \\ 0, & g \to \infty \end{cases}$$

3.4 Exercise 4

$$\begin{aligned} \widetilde{Z}_n \widetilde{X}_n &= \widetilde{Z}_n Z_{n+1} Z_n \\ &= Z_{n+1} \widetilde{Z}_n Z_n \\ &= Z_{n+1} X_n Z_n \widetilde{Z}_{n-1} \\ &= -Z_{n+1} Z_n X_n \widetilde{Z}_{n-1} \\ &= -\widetilde{X}_n \widetilde{Z}_n \end{aligned}$$

Hence, $\{\widetilde{Z}_n,\, \widetilde{X}_n\} = 0$. Performing the Kramers-Wannier duality transformation yields

$$H = -\frac{g}{2} \sum_n \widetilde{Z}_n \widetilde{Z}_{n+1} - \frac{1}{2} \sum_n \widetilde{X}_n$$

Comparing this to the original Hamiltonian

$$H = -\frac{1}{2} \sum_n Z_n Z_{n+1} - \frac{g}{2} \sum_n X_n$$

it can be seen that the Hamiltonian is (almost) self-dual, however, the coupling terms (in our case only g since we set $J = 1$) are swapped. The Hamiltonian is only self-dual when $g = 1$. This corresponds to the quantum-phase transition at $g_c = 1$. Physically this is the case, because $\left\langle \tilde{Z} \right\rangle$ is still an order parameter for the Hamiltonian with transformed operators, albeit the role of g is flipped (so it is finite for $g \to \infty$ and vanishing for $g \to 0$).

3.5 Exercise 5

Let $g = 0$. The ground states of H have no domain walls. Therefore, each domain wall costs $\Delta E = 1/2 - (-1/2) = 1$. For site j set $\varepsilon_j := \frac{1-Z_jZ_{j+1}}{2}$, which is zero if and only if there is a domain wall between site j and $j+1$. Then $H = -\frac{1}{2}\sum_{j=1}^{N} 1 - 2\varepsilon_j = -\frac{N}{2} + \sum_{j=1}^{N}\varepsilon_j \cong \sum_{j=1}^{N}\varepsilon_j$. Applying Boltzmann statistics,

$$p(\varepsilon_j) = \frac{e^{-\varepsilon_j\beta}}{1+e^{-\beta}}.$$

Therefore,

$$p(\varepsilon_j = 1) = \begin{cases} 0 & T \to 0 \\ 1/2 & T \to \infty \end{cases}$$

That is, for $T \to \infty$ we lose the ferromagnetic ordered phase. To see explicitly, that long-range ferromagnetic order cannot survive at any finite temperature $T > 0$, we consider the free energy $F = E - TS$ when creating n domain walls in a one-dimensional lattice of size N. In this case, as we have seen previously, $\Delta E = n$. The entropy gain is given by $\Delta S = k_B \log\binom{N}{n}$. Therefore, $\Delta F = \Delta E - T\Delta S = n - k_B T \log\binom{N}{n}$. Note that the energy cost does not depend on the system size unlike the entropy gain. This implies that for any $T > 0$ there exist $N > 0$ such that $\Delta S > \Delta E$, i.e. the creation of domain walls is favored and thus no long-range ferromagnetic order can be maintained. In particular, in the thermodynamic limit $N >> 1$, the energy cost does not matter compared to the entropy gain and we expect $n = N/2$, implying $\langle m_z\rangle = 0$. Hence, $T_c = 0$.

3.6 Exercise 6

We use the first order Trotterization

$$\exp\left(\hat{A}+\hat{B}\right) \approx \mathrm{e}^{\hat{A}}\mathrm{e}^{\hat{B}} \tag{11}$$

and second order Trotterization

$$\exp\left(\hat{A}+\hat{B}\right) \approx \mathrm{e}^{\hat{A}/2}\mathrm{e}^{\hat{B}}\mathrm{e}^{\hat{A}/2} \tag{12}$$

to implement the unitary time evolution of our system under the transverse field Ising Hamiltonian as

$$U(t) = \exp\left(-\mathrm{i}\hat{H}t\right) = \left(\exp\left(-\mathrm{i}\hat{H}dt\right)\right)^{t/dt} = \left(\exp\left(\hat{A}+\hat{B}\right)\right)^{t/dt} \tag{13}$$

wehere $\hat{A} = \mathrm{i}dt\frac{g}{2}\sum_i X_i$ and $\hat{B} = \mathrm{i}dt\frac{1}{2}\sum_{<i,j>} Z_iZ_j$.

We decomposed the nearest neighbour Ising interaction into two layers of two-qubit gates acting on odd and even bonds (s. Figure 12).

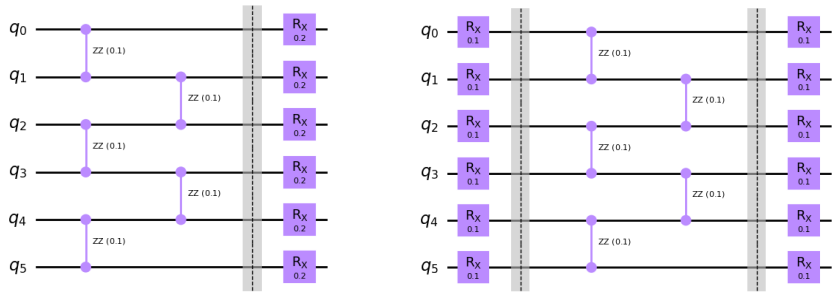

(a) first order (b) second order

Figure 12: Circuit implementation of trotterized unitary for a six qubit system.

3.7 Exercise 7

Making use of the approximated time evolution circuit we simulate a $L = 10$ body system under the transversal Ising model ($J = 1, g = 2$) for a duration of $T = 5$ and calculate the corresponding magnetization

$$m_z(t) = \frac{1}{L} \sum_i Z_i \tag{14}$$

for each time-step. Comparing the expectation values of the simulated system with the solution obtained from exact diagonalization shows almost perfect overlap (s. Figure 14b) for a increasing number of collocation points.

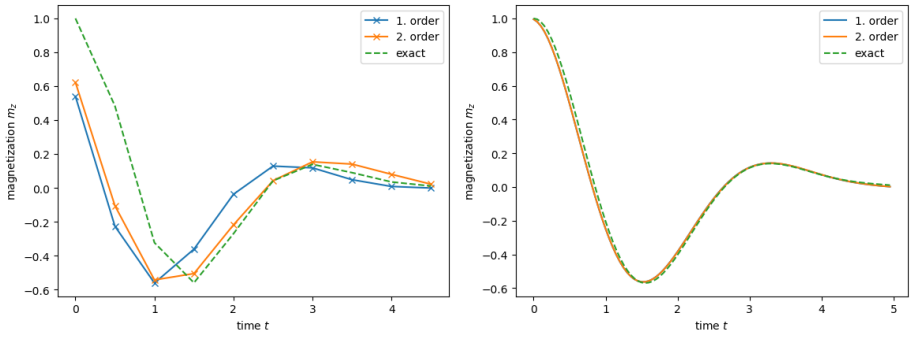

(a) $dt = 0.5$ (b) $dt = 0.05$

Figure 13: Comparision of magnetization over time for a sparse and dense sampled time grid.

3.8 Exercise 8

To extract the Loschmidt rates $\lambda_i(t)$ by projecting back onto the ground state manifold

$$\lambda_i(t) = -\frac{1}{N} \ln |\langle \Psi_i | \Psi_0(t) \rangle|^2 \tag{15}$$

we use the second order Trotterization of the unitary time evolution from the previous exercise. For different system sizes $L = 6, 8, 10, 12$ and varying values of $0.5 \leq g \leq 2$ we observe the emergence of DQPTs. The transitions seem to emerge for fixed $g = 2$ independently of the system size (characteristic peaks in Figure 14a). For a fixed $L = 6$ critical behaviour becomes visible for $g \geq 1$.

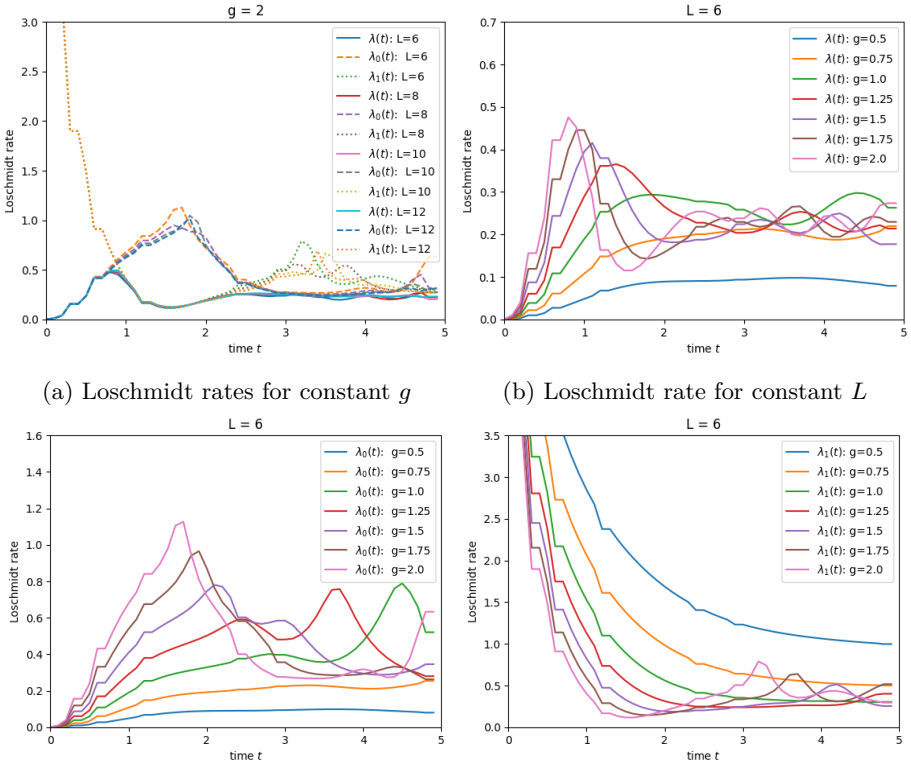

(a) Loschmidt rates for constant g

(b) Loschmidt rate for constant L

(c) λ_0 for constant L

(d) λ_1 for constant L

Figure 14: Loschmidt rates for varying system size L and coupling rate g.

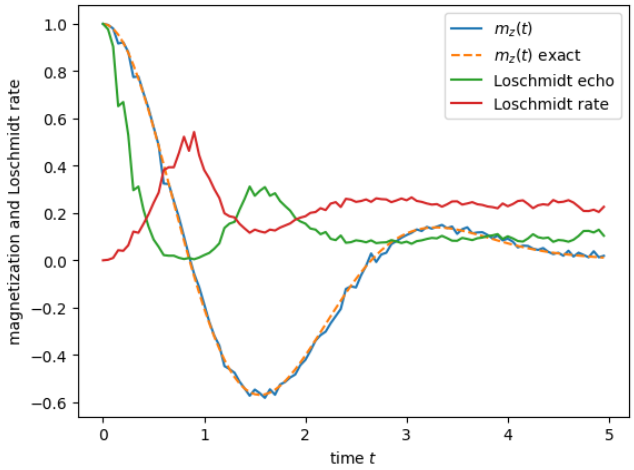

Figure 15: Comparison of Logschmidt echo, Logschmidt rate and magnetization over time t.

3.9 Exercise 9

We continue by extracting the magnetization $m_z(t)$ and Loschmidt echo $\mathcal{L}(t)$ by generating measurement data from the execution of the trotterized unitary circuit. To obtain the correct values, we repeat the run followed by a measurement for a total of $N = 2048$ shots. The lower limit for this number is depending on the system size L as there are 2^L possible measurement results we need at least $N = 2^L$ runs. Comparing the magnetization to the exact solution we can verify that the number of executions has recovered the expected behaviour.

3.10 Exercise 10

One can observe that at the critical time $t_c \approx 1.55$, both magnetization and Loschmidt rate display a (local) minimum, while the Loschmidt echo admits a local maximum.

3.11 Exercise 11

We now compute the von-Neumann entropy and the 2nd Renyi entropy. The von Neumann entropy is given by:

$$S = -\operatorname{Tr}\{\rho \log \rho\} \tag{16}$$

and the second Renyi entropy is given by:

$$S^{(2)} = -\log \operatorname{Tr}\{\rho^2\} \tag{17}$$

We are interested in the entanglement entropy. It is natural to look at the half-chain entanglement entropy (physically this just represents a measure between

the entanglement of the left and the right half of the chain). The Hilbert space of the entire system is given by $\mathcal{H} = \mathcal{H}_L \otimes \mathcal{H}_R$. Since the total density matrix is given by $\rho = |\Psi\rangle \langle\Psi|$, we look at the density matrix of left subsystem ρ_L, which is defined by:

$$\rho_L = \mathrm{Tr}_R \, \rho = \sum_j^{d_R} (I_L \otimes \langle j_R|) \, \rho \, (I_R \otimes |j_R\rangle) \tag{18}$$

It is noteworthy that $S(\rho_L) = S(\rho_R)$ and similarily for S^2. As expected it can

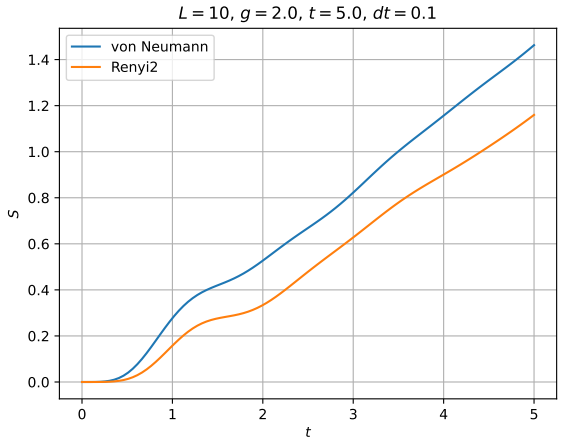

Figure 16: Comparison of the half-chain entanglement von Neumann entropy and second Renyi entropy.

be seen that the entanglement increases approximately linear with time. Since we start in a product state, the initial entanglement is zero, as (only) at zero time we can express:

$$\rho(0) = \rho_L(0) \otimes \rho_R(0) \tag{19}$$

3.12 Exercise 13

We now extract the second Renyi entropy with randomized measurements. We apply a random unitary onto each qubit (chosen all independently from the circular unitary ensemble). We then measure the qubits in the left half of the chain (corresponding to $\mathcal{H}_L$ repeatedly to aquire statistic of the distribution of the outcome strings (with length d_L). With this information we can compute the quantity

$$X = 2^{d_L} \sum_{s_L, s'_L} (-2)^{-D(s_L, s'_L)} P_U(s_L) P_U(s'_L) \tag{20}$$

where s_L, s'_L are bitstrings (of the measured qubits in the left half) with probabilities $P_U(s_L)$ ($P_U(s'_L)$), given the random unitary U was applied and $D(s_L, s'_L)$

is the Hamming distance between the two bitstrings. If this procedure is repeated for different (random) unitaries, the second Renyi entropy can be extracted by averaging over them ($\bar{X}$) and taking the negative logarithm:

$$S^2 = -\log \bar{X} \tag{21}$$

We can see that the extracted Entropy from randomized measurements does

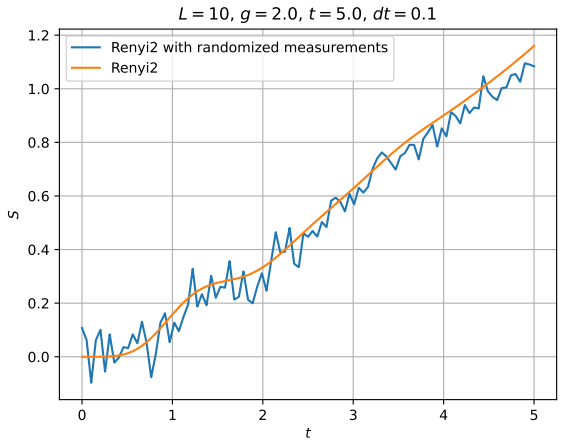

Figure 17: Comparison of the half-chain entanglement second Renyi entropy. Shown are the simulated entropy and the entropy extracted via randomized measurements.

fluctuate a lot around the simulated one. This is largely due to the fact that we only averaged over 200 different unitaries and we'd expect that the approximation get's better, once more random unitaries are used.